

# Corrosion Behavior of Hot-dip Galvanized Advanced High Strength Steel Sheet in a Simulated Marine Atmospheric Environment

Kai Zhang<sup>1</sup>, Renbo Song<sup>1,\*</sup>, Yi Gao<sup>2</sup>

<sup>1</sup> School of Materials Science and Engineering, University of Science and Technology Beijing, Beijing 100083, China

<sup>2</sup> TKAS (Chongqing) Auto Steel Company Limited, Chongqing 400000, China

\*E-mail: [songrb@mater.ustb.edu.cn](mailto:songrb@mater.ustb.edu.cn)

Received: 11 August 2018 / Accepted: 16 October 2018 / Published: 5 January 2019

---

This paper describes a study of the corrosion behavior and mechanism of 1000MPa grade hot-dip galvanized steel in a simulated marine atmospheric environment with neutral salt spray tests at different times. Subsequent weight loss measurements, electrochemical measurements, confocal scanning laser microscopy (CSLM), scanning electron microscopy (SEM) coupled with energy dispersive spectroscopy (EDS) and X-ray diffraction (XRD) were used. The results demonstrated that with neutral salt spray (NSS) time elapsing, the corrosion appearance evolved from pitting corrosion to severe uniform corrosion. At the initial time, flocculent corrosion products were predominant and were mainly made up of Zn(OH)<sub>2</sub> and ZnO. Then, the corrosion products became compact, and at this period, the corrosion rate was at a lower level, indicating that the compact products prevented the diffusion of reactive ions and were protective for the matrix. Cl<sup>-</sup> could combine with the zinc oxides and accelerate the dissolution of the protective products; ZnCl<sub>2</sub> and Zn<sub>5</sub>(OH)<sub>8</sub>Cl<sub>2</sub> · H<sub>2</sub>O were the main corrosion products. Zn<sub>5</sub>(CO<sub>3</sub>)<sub>2</sub>(OH)<sub>6</sub> develops after an extensive period of salt spray. Eventually, the compact corrosion products diminished, and the matrix was exposed and corroded.

---

**Keywords:** galvanized steel; zinc coating; salt spray; corrosion

## 1. INTRODUCTION

The corrosion behavior of steel in a marine-atmospheric environment has been a popular research topic since the wide use of steel in harsh environments with high moisture and high salinity [1-3]. Corrosion resistance can be enhanced significantly by means of galvanization, by which a zinc coating can isolate the matrix from corrosive media and act as a sacrificial anode once damaged [2,4-9]. Galvanizing technology is mainly classified into electrogalvanizing and hot-dip galvanizing [10]; hot-

dip galvanizing is more commonly used in many fields on account of lower cost, simpler manufacturing processes, thicker coatings and excellent weldability conditions [7,11].

A large number of researchers have been devoted to the study of microstructure and corrosion behavior of hot-dip galvanized steel. The better corrosion behavior of galvanized steel depends on the sacrificial zinc layer [12,13], and it is known that failure consists of three stages [14-17]: first, solid zinc corrodes; second, the corrosion products of the zinc layer grow until failing to protect the matrix; and finally, the steel corrodes. For the prevention of corrosion failures during service, it is essential to assess corrosion resistance and explore the internal corrosion mechanism, usually with indoor accelerated tests and field experiments, which have received considerable attention. Indoor accelerated tests have been developed and are now widespread, such as immersion [18], salt spray [19], and alternating wet-dry tests [20]. Liu [6] studied the effects of pH and  $\text{Cl}^-$  concentration on the corrosion behavior of galvanized steel immersed in a simulated rust layer solution, and the results showed that galvanized steel is susceptible to pitting corrosion in all concentrations of chloride solution, ranging from 0.1 to 0.6 M. Vázquez-Rodríguez C. A. [19] conducted salt spray tests on galvanized steel and characterized the corrosion products with SEM and EDS. Corrosion begins in the zinc-steel interface and then advances through a porous layer of  $\text{ZnCl}_2\cdot\text{Zn(OH)}_2$ ;  $\text{ZnO}$  and  $\text{Zn(OH)}_2$  are also generated on the porous layer; finally, iron starts to dissolve, forming  $\text{Fe}_2\text{O}_3$  and  $\text{FeOOH}$ . Electrochemical methods combined with indoor accelerated tests can provide information on the reactions and mechanisms of electrochemical deterioration. Schachinger [4] studied blister formation on coated galvanized steel in oxidizing alkaline solutions through EIS and suggested that sodium percarbonate accelerates blister growth. B. M. Fernández-Pérez [21] studied corrosion reaction at cut-edges of galvanized steel with immersion and SECM. The anodic activity initiated at the Aluzinc layer coated with the thinner organic coating, whereas alkalization of the steel related to cathodic activity was limited by the buffering ability of the soluble metal ions. In this way, precipitation of corrosion products might block the cathodic site. Field experiments are time-consuming and region-dependent and are often utilized in combination with indoor accelerated tests. Fujita [22] studied the effect of zinc and zinc-alloyed-coated sheets on perforation corrosion with field experiments in North America, specifically, with laboratory salt spray and immersion tests, finding that the main factor affecting corrosion behavior in the crevices of lapped panels was the coating weights of the zinc and zinc alloys.

Many researchers have succeeded in improving the corrosion resistance of galvanized steel by adding some alloy elements and surface treatments. E. Diler [2] characterized the corrosion products of Zn and Zn-Mg-Al (ZMA)-coated steel during a 6-month exposure in a marine environment and found that for ZMA, the addition of Al and Mg effectively improved the corrosion resistance of the zinc coating. Yadav [23] showed that the corrosion product of a 55 wt. % Al-1.6 wt. % Si-Zn-alloyed layer was more effective against oxygen transport compared with a zinc layer. An [24] treated galvanized steel with phosphating and postsealing and characterized the corrosion resistance through NSS, SEM and EIS measurement. The results showed that after treatment, porous phosphate crystals and a complete layer of silicate film formed, improving the corrosion resistance markedly. J. M. Ferreira Jr [25] prepared a new mixed organic/inorganic coating containing Ce on galvanized steel and showed superior corrosion resistance. To date, comprehensive studies on the corrosion behavior of galvanized steels have been developed. However, little effort has been focused on the corrosion behavior of galvanized steel with

ultrahigh strength and is needed for the development of steel materials and the higher performance of galvanized steel. Therefore, it is important to carry out research on 1000MPa grade hot-dip galvanized steel in a simulated marine atmosphere.

This paper describes a study of the corrosion behavior and the mechanism of 1000MPa grade hot-galvanized steel in 3.5% NaCl solution. A neutral salt spray experiment was carried out to form an indoor accelerated corrosion condition; confocal scanning laser microscopy, scanning electron microscopy coupled with energy dispersive spectroscopy and X-ray diffraction (XRD) were applied to characterize corrosion morphology and corrosion products after NSS; electrochemical measurements after salt spray and after various times were conducted to determine the variation in electrochemical properties as a function of time.

## 2. EXPERIMENTAL

### 2.1 Material and solution

Specimens in this paper were cut from a 1000MPa grade hot-dip galvanized steel sheet, of which the tensile strength reached 1029MPa. The steel matrix was dual-phased, 1.27mm thick, and coated by double side zinc layers with a thickness of  $140\text{g}\cdot\text{m}^{-2}$ . The chemical composition of the matrix and the zinc coating are shown in Table 1 and Table 2, respectively. The dimensions of the specimens used only in NSS tests were  $150\text{mm}\times 70\text{mm}\times 1.6\text{mm}$ , while those used in the electrochemical measurements were  $10\text{mm}\times 10\text{mm}\times 1.6\text{mm}$ . Prior to tests, specimens used in the electrochemical measurements were welded to a copper wire and coated with epoxy, leaving a working area of  $10\text{mm}\times 10\text{mm}$ . In specimens used only in the NSS test, the cut edges without zinc coating were coated with epoxy. Then, all the specimens were cleaned with deionized water and ethanol, followed by blow-drying.

**Table 1.** Chemical composition (wt.%) of the matrix

C	Si	Mn	V	Ti
0.16	0.67	1.72	0.072	0.015

**Table 2.** Chemical composition (wt.%) of the zinc coating

Zn	Al	Fe	Pb
99.8	0.205	0.00638	0.0031

The NSS test was conducted in 5% NaCl solution with a pH of 7.0, and the electrochemical measurements were carried out in 3.5% NaCl solution with a pH of 8.20, which is the approximate pH of seawater. All the test solutions were prepared with analytic grade reagents and deionized water.

## 2.2 NSS test

The NSS test was conducted with a salt spray corrosion test chamber for 120h. Continuous spray was employed; the temperature was  $35\pm 2^\circ\text{C}$ . The placement of the specimens was at an angle of  $20\pm 5^\circ$  with respect to the vertical direction. After salt spray for various periods of time (0h, 6h, 24h, 30h, 48h, 72h, 96h and 120h), the specimens used only in the NSS test were taken out, and the corrosion morphology was examined with a digital camera and SEM. The composition of the corrosion products was analyzed with XRD on a Bruker D8 Advance X-ray diffractometer with a Cu target, a working voltage of 40kV, a current of 40mA, a scanning step of  $0.04^\circ$ , a scanning rate of 6/min, and the  $2\theta$  ranging from  $10^\circ$  to  $90^\circ$ . Rust was removed with a descaling liquid (prepared with 200g  $\text{CrO}_3$ +1000mL deionized water), after which the specimens were cleaned with deionized water and ethanol and blow-dried. After rust removal, CSLM was applied to examine the corrosion morphology. An electronic balance was used to measure their weight, and then, the corrosion rate was calculated according to the following formula:

$$v = \frac{w_0 - w_t}{S \cdot t} \quad (1)$$

where  $t$  represents the time of salt spray,  $w_0$  and  $w_t$  are the weight before and after salt spray and followed by rust removal, and  $S$  is the exposed area of the specimen.

## 2.3 Electrochemical measurements

After salt spray for various periods of time (0h, 6h, 24h, 30h, 48h, 72h, 96h and 120h), the specimens to be used for electrochemical measurements were removed. The electrochemical measurements were conducted with a Princeton VersaSTAT Multichannel electrochemical workstation. A conventional three-electrode system was used, in which the specimen acted as the working electrode, a platinum gauge acted as the counter electrode, and a saturated calomel electrode (SCE) acted as the reference electrode.

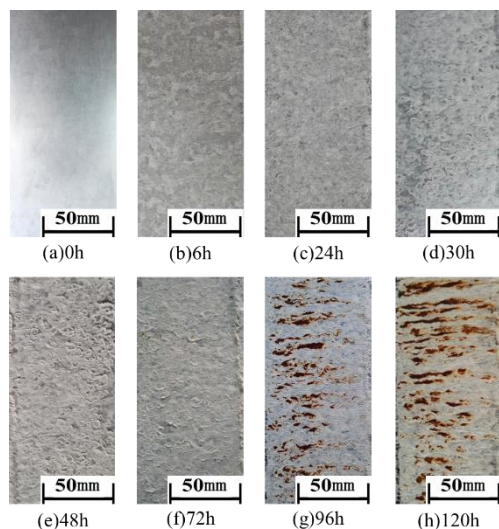
At the beginning of the tests, the specimens were immersed in the test solution until the open circuit potential (OCP) reached stability. Later, electrochemical impedance spectroscopy (EIS) was measured with an AC perturbation of 10mV (vs. OCP) at the measuring frequency of 0.01-100000Hz. The results were fitted with ZsimpWin software. All the electrochemical tests were performed at ambient temperature ( $22^\circ\text{C}$ ) and repeated three times to guarantee reliability and repeatability of the data.

# 3. RESULTS AND DISCUSSION

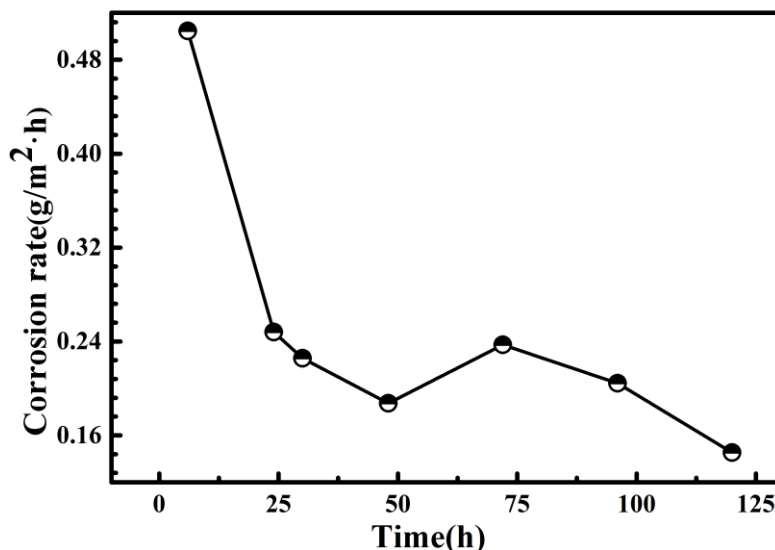
## 3.1 Corrosion morphology of the galvanized steel after the NSS tests

Fig. 1 shows the macro-corrosion morphology of the specimens after NSS and after various times. Before salt spray, the surface of the specimen is intact and bright. After 6h of NSS, the zinc coating is slightly corroded; some white spots develop, and the metallic luster disappears. With time passing, the degree of corrosion becomes increasingly more severe. Particularly, white corrosion products cover almost the whole surface at 48h and 72h, demonstrating uniform corrosion of the zinc coating. Red rust

can be observed at 96h, where zinc failed to protect the matrix from corrosion. At 120h, the entire matrix is exposed and heavily corroded.



**Figure 1.** Macro-corrosion morphology of the specimens after NSS and after various times (a) 0h; (b) 6h; (c) 24h; (d) 30h; (e) 48h; (f) 72h; (g) 96h; (h) 120h.



**Figure 2.** Corrosion rate of the specimens during NSS after various times.

Fig. 2 illustrates the corrosion rate of the specimens during NSS after various times, showing first an increase and then a decrease. Combined with the corrosion morphology, at the first 30h, zinc is corroded at a high corrosion rate due to the direct contact between the zinc coatings and the corrosive medium, and as time passes, the degree of corrosion of the zinc coating becomes increasingly greater. This stage is called the initial corrosion stage of galvanized steel reported in the literature [26]. At 48h, compact and protective corrosion products form, in which the corrosion rate is the lowest; at 72h, there is a minor increase in the corrosion rate, which may be attributed to the consumption of the protective corrosion products. Then, the matrix begins to be exposed, the corrosion rate of which is lower and may account for the subsequent descending curve. The variation in the corrosion rate is considered to be

related to the types of corrosion products, especially the compactness and adhesive property [27], which is discussed further in 3.3.

For assessing the corrosion form, the specimens for NSS tests after rust removal were observed with CSLM (Fig. 3), which illustrates the initiation and development of corrosion with NSS time passing. In the initial period, the zinc coating is corroded, and the corrosion appearance is mainly pitting corrosion with the pit diameter ranging from 1.5 $\mu$ m to 2.5 $\mu$ m. With the passage of time, the pits multiply rapidly and grow in depth instead of in the radial direction, and this outcome is in agreement with results reported in the literature [27]; the pits gradually become confluent and eventually transform to present severe uniform corrosion.

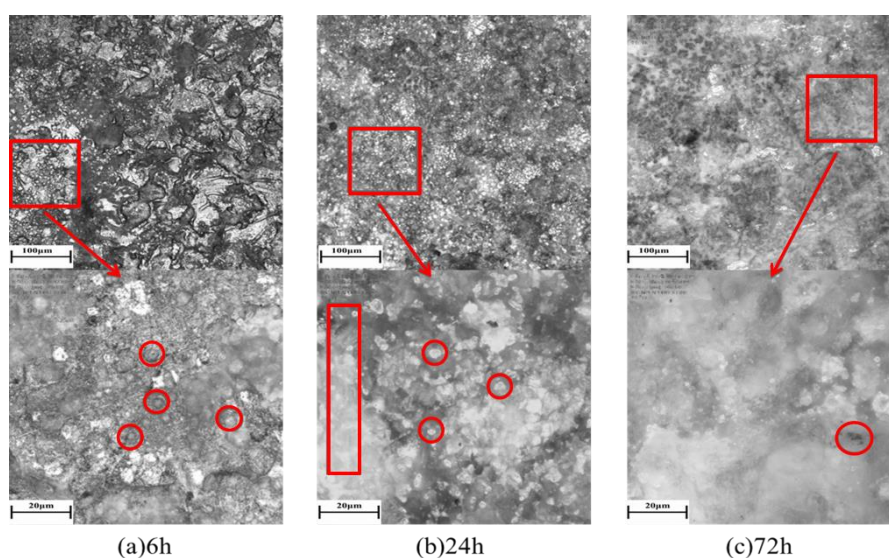


**Figure 3.** Corrosion morphology of galvanized steel after rust removal (a) 6h; (b) 24h; (c) 72h.

### 3.2 Electrochemical behavior of galvanized steel during NSS

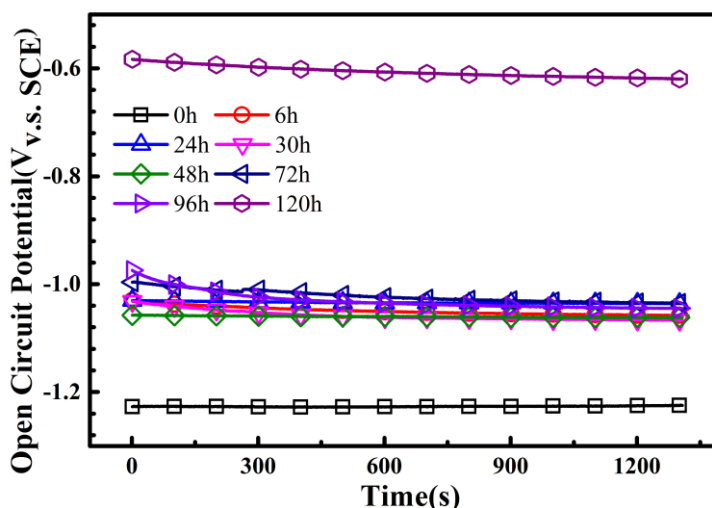


**Figure 4.** OCP of galvanized steel after the NSS test and after various times.

Fig. 4 shows the OCP of galvanized steel after NSS testing over a range of various times. The results show that after salt spray, the OCP shifted positively and significantly; this outcome is attributed to the damage of the zinc coating and thus the galvanic corrosion between zinc and the steel matrix. In addition, the OCP varies slightly (approximately -1.05V) in the first 96h and then exerts an obvious positive shift to approximately -0.6V after 120h NSS, reaching the corrosion potential of steel materials in 3.5% NaCl solution. Therefore, it can be inferred that most of the zinc coating is totally destroyed, and the exposed steel matrix suffers from severe chloride-induced corrosion, which corresponds well with the corrosion morphology observation and can be verified with the XRD results.

As is known, the EIS technique has been extensively used to characterize surface coatings in a semiquantitative way [4,28]. The EIS diagrams of galvanized steel are displayed in Fig. 5. It can be seen that the EIS diagram demonstrates characteristics of two time constants. It can be inferred that a complicated mass transport mechanism participates in the corrosion process [7]. In the EIS diagram, the high-frequency part is related to charge transfer, associated with the effect of an electric double-layer, while the low-frequency part characterizes a finite thickness diffusion process, mainly depending on the properties of the corrosion products. After the first 30h, the corrosion process was controlled by the active dissolution of zinc, while at 48-72h, the emergence of the diffusive tail at low frequency indicates the mixed control of diffusion and active dissolution. Finally, at 96-120h, the corrosion process is controlled by the active dissolution of the matrix. Combined with the macro-corrosion morphology in 3.1, it can be inferred that at 48-72h, the intact corrosion products of zinc prevented the diffusion of reactive ions; while at 96-120h, the matrix was exposed and corroded. Similar results also appear in Liu’s work [28], demonstrating that with the passage of immersion time, the low-frequency arc in the Nyquist diagram shrinks; this shrinkage results from the complete blockage of the pores in the outer coarse layer by the accumulation of the corrosion products. Further, as immersion time increases, the maximum phase angle at high frequency increases, indicating that the corrosion products become more compact.

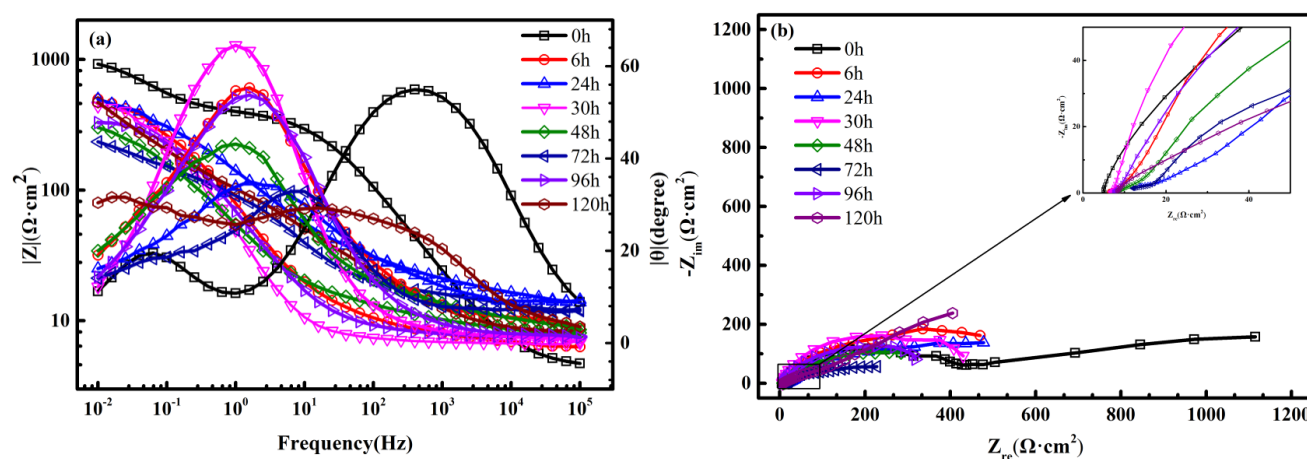
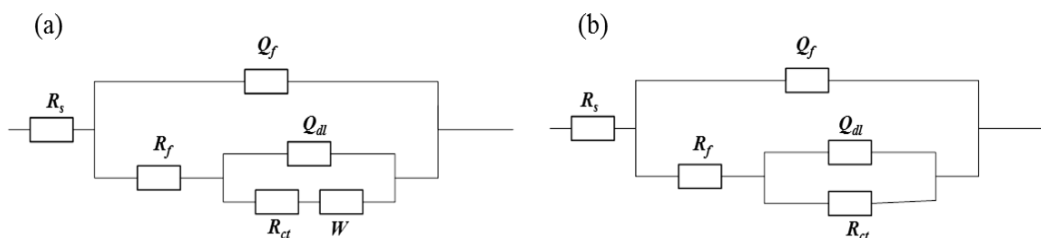


Figure 5. EIS diagram of galvanized steel after the NSS test after various times: (a) Bode; (b) Nyquist.

The software of ZSimpWin was used to fit the EIS plots, and two models of  $R_s(Q_f(R_f(Q_{dl}R_{ct})))$  and  $R_s(Q_f(R_f(Q_{dl}(R_{ct}W))))$  were applied to analyze the variation in corrosion progress, as shown in Fig. 6. The fitted values are shown in Table 3.



**Figure 6.** Equivalent circuit diagram: (a)  $R_s(Q_f(R_f(Q_{dl}R_{ct})))$  model; (b)  $R_s(Q_f(R_f(Q_{dl}(R_{ct}W))))$  model.

$R_s$  is the solution resistance from the reference electrode to the working electrode;  $R_{ct}$  and  $Q_{dl}$  are the constant phase elements (CPE) of the charge transfer resistance and the angle element of the electric double-layer capacitor between the solution and the matrix;  $R_f$  and  $Q_f$  stand for the resistance and CPE between the solution and the zinc coatings. A Warburg impedance,  $W$ , was used to fit the plateau of the phase angle at low frequency. In general, the capacitor of the electric double layer cannot be considered as the ideal capacitive element because of the roughness of the electrode surface, the impedance of which is always concerned with the angular frequency of the pumping signals and conveyed in the following form:

$$Z_{dl} = \frac{1}{Y_0(j\omega)^n} \quad (2)$$

where  $Y_0$  is a proportional factor,  $\omega$  is the angular frequency,  $j$  is the symbol for the imaginary unit, and  $n$  represents the index of the constant phase angle element.

**Table 3.** Fitted values of the equivalent circuit of the EIS diagram.

Time, h	$R_s, \Omega \cdot \text{cm}^2$	$\frac{Q_f,}{\Omega^{-1} \text{cm}^{-2} \text{s}^n}$	n	$R_f, \Omega \cdot \text{cm}^2$	$\frac{Q_{dl},}{\Omega^{-1} \text{cm}^{-2} \text{s}^n}$	n	$R_{ct}, \Omega \cdot \text{cm}^2$	$\frac{W,}{\Omega \cdot \text{cm}^2 \text{s}^{1/2}}$
0	4.318	$7.897 \times 10^{-5}$	0.73	406.5	$5.786 \times 10^{-3}$	0.79	634.9	-
6	6.289	$2.823 \times 10^{-3}$	0.56	8.962	$1.009 \times 10^{-3}$	0.89	646.1	-
24	1.089	$1.829 \times 10^{-3}$	0.39	2.307	$1.031 \times 10^{-3}$	0.63	706.2	-
30	6.689	$3.314 \times 10^{-3}$	0.77	2.260	$1.187 \times 10^{-3}$	1.00	455.33	-
48	7.671	$4.088 \times 10^{-3}$	0.48	1.203	$2.341 \times 10^{-3}$	0.79	388.9	272.81
72	2.594	$6.958 \times 10^{-3}$	0.17	2.249	$6.804 \times 10^{-4}$	0.79	2.475	83.29
96	7.687	$3.766 \times 10^{-3}$	0.73	373.2	$2.713 \times 10^{-1}$	1.00	120.2	-
120	7.613	$2.219 \times 10^{-3}$	0.50	135.6	$6.827 \times 10^{-3}$	0.52	1686	-

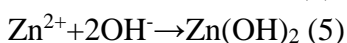
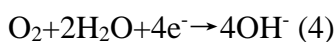
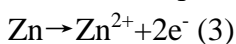
### 3.3 Corrosion products of the galvanized steel after the NSS tests.

Fig. 7 shows the morphology and element distribution of the corrosion products of galvanized steel after NSS. Before NSS, the surface is intact, with few coating defects and no corrosion products; Zn is evenly distributed. After 6h NSS, flocculent and loose corrosion products are created and are verified to be zinc oxides by EDS mapping. When the NSS time reaches 24h, masses of corrosion products appear, where Cl is enriched and O is depleted. According to Ohtsuka [29], the destructive effect of Cl<sup>-</sup> on zinc oxides causes less severe flocculent corrosion products. In the first 30h, the corrosion products are loose and not protective, accounting for the increase in corrosion rate in Fig. 2. At 48h, compact corrosion products such as plate strips form and are adherent to clusters on the surface or within the crevice; O and Zn are distributed uniformly, and no Fe is detected. The compact corrosion products prevent the attack of corrosive media and lead to the plateau of the corrosion rate. With the time elapsing, the zinc coating is continuously destroyed, clusters gradually diminish, and the plate strips are pitted with cracks and subsidence holes. Especially at 96h, clusters are rare; the remaining corrosion products are further corroded and exert a gap-shape, in which a large amount of Cl is detected. It can be inferred that the damage of the plate strips is related to Cl<sup>-</sup>. At 120h, the existence of Fe demonstrates the comprehensive damage of the zinc coating and the corrosion of the matrix. The transformation of the corrosion products corresponds with the variation in macro morphology (Fig. 1), corrosion rate (Fig. 2) and electrochemical curves.

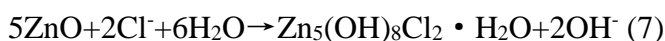
For understanding the chemical composition of corrosion products, XRD analysis was conducted. From Fig. 8, at the initial NSS time, amorphous Zn(OH)<sub>2</sub> appears, transforms to β-Zn(OH)<sub>2</sub> and then changes into ZnO rapidly from dehydration. At 48h, Zn<sub>5</sub>(OH)<sub>8</sub>Cl<sub>2</sub>·H<sub>2</sub>O comes into being as a result of the combination of Cl<sup>-</sup> and zinc oxides; furthermore, Zn<sub>5</sub>(CO<sub>3</sub>)<sub>2</sub>(OH)<sub>6</sub> is observed. When NSS time reaches 120h, a substantial amount of Fe<sub>2</sub>O<sub>3</sub> is detected.

On the basis of Santos's work [10], the corrosion mechanism during NSS can be summarized in Fig. 9, and the chemical reactions are shown as follows:

At the initial period (0-6h):



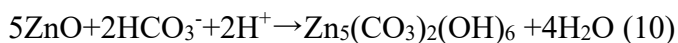
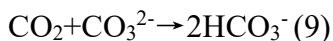
Afterwards, Cl<sup>-</sup> migrates and destroys zinc oxides in the following formula at 24h, and Zn<sub>5</sub>(OH)<sub>8</sub>Cl<sub>2</sub> · H<sub>2</sub>O begins to appear:



At 48h and 72h, an increasing amount of Zn<sub>5</sub>(OH)<sub>8</sub>Cl<sub>2</sub> · H<sub>2</sub>O forms and accumulates in the bottom part of the pits, and it is considered to be able to repel aggressive ions and mitigate further corrosion processes [30].

Zinc hydroxide carbonate was detected after 72h immersion and was generally considered to be present in the outer layer of the corrosion products [31]. The formation of the carbonate was considered to depend on the absorption of atmospheric carbon dioxide into the surface electrolyte and the formation of carbonate and bicarbonate, as (8)~(10) shows [28]. The carbonate was quite porous and had a low

ability to hinder the transport of oxygen and water to the metal surface, facilitating further propagation of the localized corrosion attack.



Eventually, the zinc coating is consumed and cannot provide sacrificial anodic protection; the matrix is exposed and corroded, manifesting as red rust (at 120h):

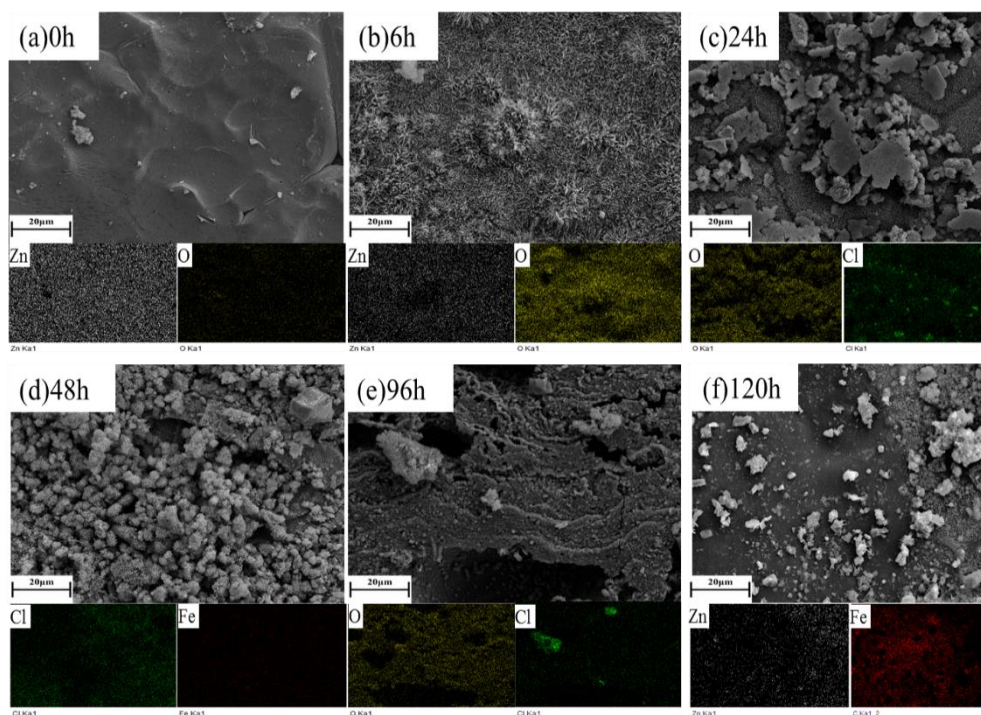
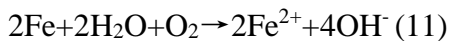


**Figure 7.** Corrosion morphology and element distribution of the corrosion products of the galvanized steel after NSS (a) 0h; (b) 6h; (c) 24h; (d) 48h; (e) 96h; (f) 120h.

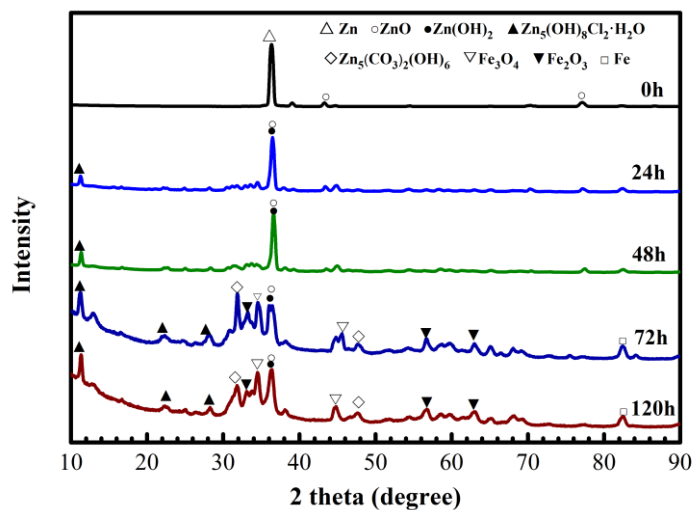


**Figure 8.** XRD diagram of the corrosion products of the galvanized steel after NSS.

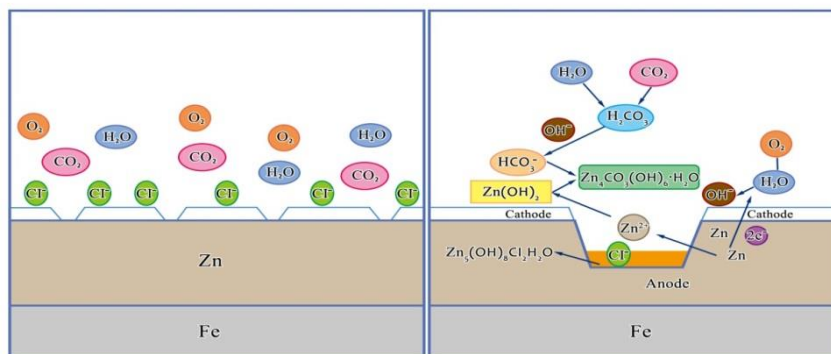


**Figure 9.** Schematic diagram of the corrosion mechanism of the specimens during NSS.

#### 4. CONCLUSIONS

The main conclusions from this study are summarized below:

With NSS time elapsing, the corrosion appearance evolves from pitting corrosion to severe uniform corrosion. At an initial time, flocculent corrosion products are predominant and are mainly made up of  $Zn(OH)_2$  and  $ZnO$ . Then, the corrosion products become compact, and during this period, the corrosion rate is at a lower level, while the corrosion current density is the lowest. This outcome indicates that the compact products prevent the diffusion of reactive ions and are protective for the matrix. The combination of  $Cl^-$  and zinc oxides accelerates the dissolution of the protective products, and  $ZnCl_2$  and  $Zn_5(OH)_8Cl_2 \cdot H_2O$  are the main products. After 72h NSS,  $Zn_5(CO_3)_2(OH)_6$  is created; gradually, the compact corrosion products diminish, and the matrix is exposed and corroded.

#### References

1. H. Ma, Z. Liu, C. Du, X. Li, Z. Cui, *Mater. Sci. Eng. A*, 650 (2016) 93.
2. E. Diler, B. Rouvellou, S. Rioual, B. Lescop, G. Nguyen Vien, D. Thierry, *Corros. Sci.*, 87 (2014) 111.
3. G. R. Meira, C. Andrade, E. O. Vilar, K. D. Nery, *Constr. Build. Mater.*, 55 (2014) 289.
4. E. D. Schachinger, R. Braidtb, B. Strau, A. W. Hassel, *Corros. Sci.*, 96 (2015) 6.
5. M. Reichinger, W. Bremser, M. Dornbusch, *Electrochim. Acta*, 231 (2017) 135.
6. S. Liu, H. Sun, L. Sun, H. Fan, *Corros. Sci.*, 65 (2012) 520.
7. E. A. Alvarenga, V. F. Lins, *Surf. Coat. Tech.*, 306 (2016) 428.
8. I. Aslam, B. Li, R. L. Martens, J. R. Goodwin, H. J. Rhee, F. Goodwin, *Mater. Charact.*, 120 (2016) 63.
9. Y. Miyoshi, J. Oka, S. Maeda, *Transactions ISIJ*, 23 (1983) 974.
10. A. P. Santos, S. M. Manhabosco, J. S. Rodrigues, L. F. Dick, *Surf. Coat. Tech.*, 279 (2015) 150.
11. P. R. Seré, C. Deyá, C. I. Elsner, A. R. D. Sarli, *Procedia Mater. Sci.*, 8 (2015) 1.
12. A. P. Yadav, A. Nishikata, T. Tsuru, *Corros. Sci.*, 46 (2004) 169.
13. A. P. Yadav, A. Nishikata, T. Tsuru, *Corros. Sci.*, 46 (2004) 361.
14. G. A. Mahdy, A. Nishikata, T. Tsuru, *Corros. Sci.*, 42 (2000) 183.
15. F. Thebault, B. Vuillemin, R. Oltra, K. Ogle, C. Allely, *Electrochim. Acta*, 53 (2008) 5226.
16. F. Thebault, B. Vuillemin, R. Oltra, C. Allely, K. Ogle, *Electrochim. Acta*, 56 (2011) 8347.

17. S. J. Pantazopoulou, K. D. Papoulia, *Eng. Mech.*, 127 (2001) 342.
18. N. S. Azmat, K. D. Ralston, B. C. Muddle, I. S. Cole, *Corros. Sci.*, 53 (2011) 1604.
19. C. A. Vázquez-Rodríguez, D. L. Garza-Garza, C. G. Tiburcio, B. E. Maldonado, M. A. Baltazar-Zamora, C. R. Garza, R. O. García, N. F. Garza-Montes-de-Oca, R. J. Ramirez, F. Almeraya-Calderón, *Int. J. Electrochem. Sci.*, 10 (2015) 4654.
20. O. E. Barcia, O. R. Mattos, N. Pebere B. Tribollet, *J. Electrochem. Soc.*, 140 (1993) 2825.
21. B. M. Fernández-Pérez, J. Izquierdo, J. J. Santana, S. González, R. M. Souto, *Int. J. Electrochem. Sci.*, 10 (2015) 10145.
22. S. Fujita, D. Mizuno, *Corros. Sci.*, 49 (2007) 211.
23. A. P. Yadav, A. Nishikata, T. Tsuru, *ISIJ Int.*, 44 (2004) 1727.
24. K. An, C. An, C. Yan, Y. Qing, Y. Shang, C. Liu, *Int. J. Electrochem. Sci.*, 12 (2017) 2102.
25. J. M. Ferreira Jr., J. L. Rossi, M. A. Baker, S. J. Hinder, I. Costa, *Int. J. Electrochem. Sci.*, 9 (2014) 1827.
26. Z. Q. Tan, C. M. Hansson, *Corros. Sci.*, 50 (2008) 2512.
27. X. Zhang, *Br. Corros. J.*, 32 (1997) 28.
28. Y. Liu, H. Y. Li, Z. G. Li, *Int. J. Electrochem. Sci.*, 8 (2013) 7753.
29. T. Ohtsuka, M. Matsuda, *Corros.*, 59 (2003) 407.
30. H. B. Zeng, J. G. Dai, W. H. Li, C. S. Poon, *Constr. Build. Mater.*, 166 (2018) 572.
31. D. Persson, D. Thierry, O. Karlsson, *Corros. Sci.*, 126 (2017) 152.

© 2019 The Authors. Published by ESG ([www.electrochemsci.org](http://www.electrochemsci.org)). This article is an open access article distributed under the terms and conditions of the Creative Commons Attribution license (<http://creativecommons.org/licenses/by/4.0/>).